

Simulation of Third-Integer Resonant Extraction of 800 MeV Protons in the Delivery Ring

Axel Moreen

Lewis University, Romeoville, IL 60446, USA

Abstract

This project presents a simulation of third-integer resonant extraction of 800 MeV protons in the Delivery Ring to extend current Mu2e infrastructure to proposed experiments that require low-energy proton beams under 2 GeV. An overview of third-integer extraction, its application to the Delivery Ring, and considerations made for extracting 800 MeV protons are discussed. Choice of ring parameters and preliminary tracking results are given.

This work was supported in part by the U.S. Department of Energy, Office of Science, Office of Workforce Development for Teachers and Scientists (WDTs) under the Science Undergraduate Laboratory Internships Program (SULI).

Introduction

Part of the Fermilab's Accelerator Division Muon Department Mission Statement[1] is to: "repurpose, redesign, rebuild, and upgrade the former Antiproton Source beam lines and rings...for use with future Muon Campus experiments." Currently, the Delivery Ring[2], repurposed from the Tevatron[3] project, is tuned to provide 3 GeV muon and 8 GeV proton beams for the g-2 and Mu2e[5] experiments, respectively. However, there is motivation to upgrade the Delivery Ring to facilitate future proposed experiments, which would require deceleration of the injected beam to low energies[4] and slow spill extraction of the low energy particles. Third-integer resonant extraction is the technique employed by the Mu2e experiment to perform slow spill extraction, allowing particles to be extracted over variably long timeframes. The purpose of this paper is to present Delivery Ring tracking simulations that extend resonant extraction to 800 MeV protons.

Overview of Third-Integer Extraction

This section will go over the theory of third-integer resonant extraction, which can be found in textbooks, for example [6]. Sextupoles (and other higher-ordered multipoles) have a non-linear effect on a particle's trajectory with respect to amplitude of betatron oscillation. For example, the expansion of an upright magnetic multipole is:

$$\frac{e}{cp} B_y = \hbar + kx + \frac{1}{2}mx^2 + \frac{1}{6}rx^3 + \dots \quad (1)$$

where the terms shown on the right-hand side (in order) are dipole, quadrupole, sextupole, and octupole contributions to the magnetic field. For the sake of this paper, higher-order effects from working with real magnets, eddy currents, and fringe fields are ignored. So, a magnet will be here approximated by its first-order effect; a dipole magnet only contributes a dipole (constant) field, a quadrupole magnet contributes a quadrupole (linear) field, and so on. As relevant to third-integer extraction, normal sextupoles have a vector potential[7]

$$A_s = -\frac{1}{3!} \frac{\partial^2 B_y}{\partial x^2} (x^3 - 3xy^2) \quad (2)$$

in the coordinate system where s is the longitudinal direction of motion and x and y are amplitudes of betatron oscillation in the local horizontal and vertical directions, respectively. To excite a resonance, the horizontal and vertical lattice tunes should satisfy[6]

$$M\nu_x + N\nu_y = P \quad (3)$$

with integers $|M| + |N|$ summing to the order of resonance and with P as an arbitrary integer. If both M and N have the same sign as P , the resonance is unstable and uncoupled in the x and y directions. For the case of unstable third-order resonances, the following combinations of tunes ν_x and ν_y are possible[6]:

$$3\nu_x = P \quad (4)$$

$$2\nu_x + \nu_y = P \quad (5)$$

$$\nu_x + 2\nu_y = P \quad (6)$$

$$3\nu_y = P \quad (7)$$

The Delivery Ring is currently designed to extract for the first of these four cases, equation 4, where the third-order resonance is excited in the horizontal direction and the vertical direction is ignored. So, y in eq. 2 can be set to zero, and \mathbf{B} is then calculated from eq. 2

$$\mathbf{B} = \nabla_x \mathbf{A} = -\frac{\partial}{\partial x} A_s \hat{y} = \frac{1}{2} \frac{\partial^2 B_y}{\partial x^2} x^2 \hat{y} \quad (8)$$

which can be simply related to eq. 1.

$$m = \frac{\partial^2 B_y}{\partial x^2} \quad (9)$$

In MAD-X [8], the program used in this paper for particle tracking, m is related to sextupole coefficient K_2 by

$$K_2 = \frac{1}{(B\rho)} \frac{\partial^2 B_y}{\partial x^2} \quad (10)$$

So,

$$m = (B\rho)K_2 \quad (11)$$

where $B\rho$ is the ‘‘magnetic rigidity’’ of the particle ($B\rho = p_s/q$) and K_2 is the sextupole coefficient used for tracking.

In a ring, the sextupoles create resonances if the machine tune is near a third-integer, prescribed for us by equation 4. The Hamiltonian for this case is approximately[9]:

$$H = (\delta Q)J + sJ^{3/2} \cos(\delta) \quad (12)$$

where δQ is a small “tune separation” from the third-integer tune $\delta Q = \frac{P}{3} - \nu_x$, J is an action-angle coordinate given by

$$J_x = \frac{1}{2\beta_x} [x^2 + (\beta_x x' + \alpha_x x)^2], \quad (13)$$

or in normalized coordinates where position $(x_N, x'_N) = \left(\frac{x}{\sqrt{\beta}}, \frac{\alpha x + \beta x'}{\sqrt{\beta}} \right)$,

$$2J_x = x_N^2 + x'_N{}^2. \quad (14)$$

α_x and β_x are Courant-Snyder parameters in the horizontal direction, observation location ψ is assumed to be zero, δ is a phase-offset that corresponds to the position of the effective sextupole in the ring from observation, and s is a sum of resonant sextupole effects around the ring:

$$se^{i\delta} = \frac{\sqrt{2}}{24\pi} e^{3i(\psi+2\pi[\delta Q]N)} \int_0^C \beta_x^{3/2}(s) \frac{\partial^2 B_y}{\partial x^2} e^{3i\phi(s)} ds \quad (15)$$

The Hamiltonian in equation 12 is linear for $s = 0$ and describes perturbations in the ring as the sextupole strength is increased. By ramping the sextupoles adiabatically, horizontal phase space given by this Hamiltonian in normalized coordinates distorts from a circular distribution into a triangle, as seen in Figure 1. There are three unstable fixed points of motion in the system:

$$J_0 = \frac{2\delta Q}{3s} \quad (16)$$

$$\phi_0 = 0, 2\pi/3, -2\pi/3 \quad (17)$$

for the tune separation we are studying ($\delta Q > 0$) in J, ϕ action-angle coordinates. The unstable fixed points make the vertices of an equilateral triangle, seen in Figures 6-8, and the edges of the triangle are the separatrices of the Hamiltonian.

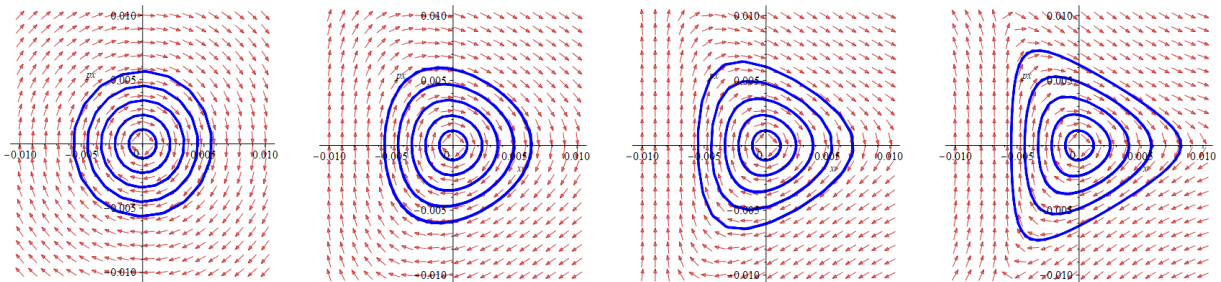


Figure 1. Example contour map of horizontal phase space distorting into a triangular shape as sextupoles are ramped from zero strength. Pictures left to right give contour lines of constant action J in normalized phase-space for increasing s .

Resonant extraction has an advantage over single-turn extraction in that the particles can be squeezed out of the machine over many turns, therefore being useful to a host of experiments with different specifications for spill rate. In the simulations presented, particles were extracted by decreasing the tune separation δQ to zero. The squeeze is done by introducing a family of 0th harmonic (tune shift) quadrupoles:

$$q_0 = \frac{1}{4\pi} \sum_i \frac{\partial B_y}{\partial x} \frac{1}{B\rho} l_i \beta_i \quad (18)$$

With length of magnet l_i and beta function β_i at each quadrupole. Now tune separation can be replaced with Δ

$$\Delta = \delta Q - q_0 \quad (19)$$

with the intention of ramping $\Delta \rightarrow 0$ by increasing q_0 . This has the effect of shrinking stable phase space until the beam has been extracted, as is seen in Figure 12. Note the tracking study performed ramped q_0 linearly, which results in a nonlinear spill rate (a constant spill rate with linear ramp would imply a uniform density across the beam, which is *not* the case—see Figure 16b from the Appendix).

Delivery Ring Lattice

The Delivery Ring has 57 FODO cells that make up three-fold symmetry, with three mirror-symmetric “straight” sections. Each “arc” section has 11 bending cells and 2 missing-dipole dispersion suppression cells so that the straights are dispersion free—this allows ignoring chromatic effects from the extraction sextupoles. There are also chromaticity correcting sextupoles in the arc sections, which are unrelated to resonant extraction. The straight sections each have 6 cells. Among the straights are two extraction sextupole families and tune quadrupoles placed optimally to perform resonant extraction. The machine tunes for the ring are $\mu_x = 9.65$ and $\mu_y = 9.485$. In extraction, μ_x is ramped by 0th harmonic quadrupoles until $\mu_x = 9.666\dots$, on the third-integer. Illustrations of the Delivery Ring layout and third-integer extraction placements can be found in Figures 2 and 3.

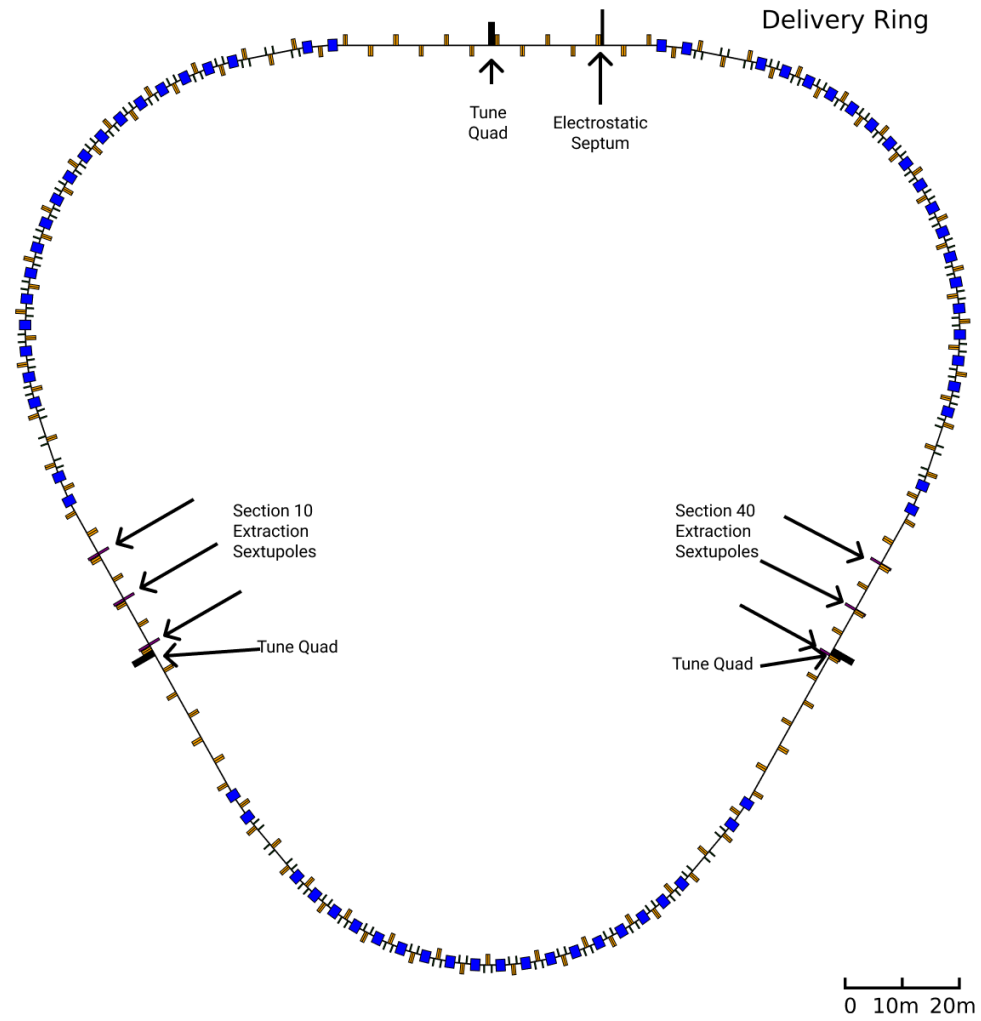


Figure 2. Layout of the Delivery Ring (magnet widths perpendicular to the length of ring are not to scale) illustrating the three-fold symmetry. The sextupoles, tune quadrupoles and the electrostatic septum used for extraction are labeled in the diagram.

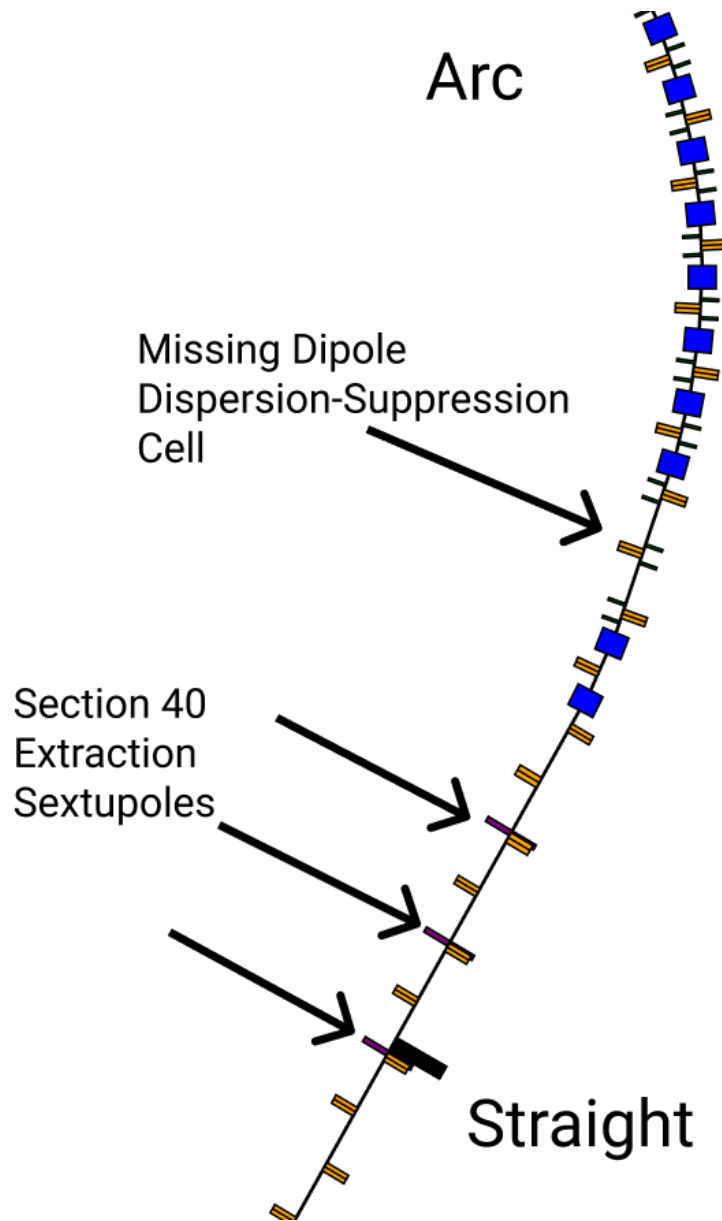


Figure 3. Zooming in on a sector of the Delivery Ring illustration in Figure 2, which is composed of half an arc section and half a straight section. Shown with an arrow is the missing dipole dispersion suppression cell.

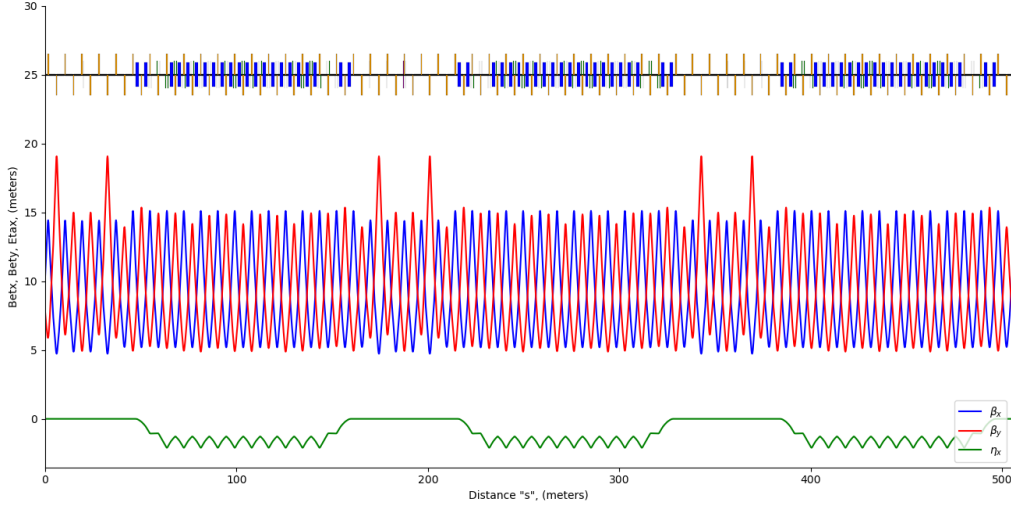


Figure 4. Courant-Snyder (Twiss) parameters of the Delivery Ring. Magnetic element locations are indicated along the top axis – boxes centered on the axis are dipoles, taller orange elements extending up and down are focusing and defocusing quadrupoles, respectively.

Sextupole Families and Rotation of Phase Space

The sextupole resonances described by equation 15 can be written[10] as a summation of discrete sextupoles from sine and cosine contributions at locations ψ_i where sextupoles with lengths l_i are placed.

$$s_s = \frac{1}{4\pi} \sum_i \frac{\partial^2 B_y}{\partial x^2} \frac{l_i}{6B\rho} \beta_i^{3/2} \sin(3\psi_i) \quad (20)$$

$$s_c = \frac{1}{4\pi} \sum_i \frac{\partial^2 B_y}{\partial x^2} \frac{l_i}{6B\rho} \beta_i^{3/2} \cos(3\psi_i) \quad (21)$$

These contributions can be visualized with a phasor diagram, which is used in figures 5 and 15. The amplitude of each phasor is the sine contribution and cosine contribution added in quadrature:

$$s_i = \sqrt{s_{si}^2 + s_{ci}^2} \quad (22)$$

and the angle for each phasor is:

$$\tan(\chi_i) = \frac{s_{si}}{s_{ci}}$$

Each contribution is vector-like in the orthogonal directions \hat{s}_s and \hat{s}_c , so that the total sextupole strength in the ring adds

$$s = \sqrt{s_s^2 + s_c^2} \quad (23)$$

and has the angle:

$$\tan(\chi) = \frac{s_s}{s_c} \quad (24)$$

Together, the sextupoles in the ring behave as though they were one sextupole with strength s and phase offset χ .

In theory, one could create a family of sextupoles with reinforcing contributions if $\Delta v_x \psi_i = \Delta \phi$ were 60° between sextupoles, the polarity of the gradients were altered, and β were the same at each location. By 60° phase separation, one has $0, \pi, 2\pi \dots$ rotated phasors within a sextupole family. Note that $\sin(n\pi + \delta) = \sin(n\pi)\cos(\delta) + \cos(n\pi)\sin(\delta) = \sin(\delta) - \sin(\delta) + \sin(\delta) \dots$ for increasing $n \geq 0$, so by flipping the sign of the sextupole gradient for the odd n phasors, the contributions can be made to add up to $n \sin(\delta)$. Similarly, $\cos(n\pi + \delta) = \cos(n\pi)\cos(\delta) + \sin(n\pi)\sin(\delta) = \cos(\delta) - \cos(\delta) + \cos(\delta) \dots$ and is made to be $n \cos(\delta)$ by again, alternating the sign of the sextupole gradient.

By using two orthogonal families of sextupoles (separated by an odd multiple of 30° phase advance), the sine and cosine contributions in equations 20 and 21 can then be replaced:

$$s_1 = \frac{n}{4\pi} \frac{\partial^2 B_y}{\partial x^2} \frac{l}{6B\rho} \langle \beta^{3/2} \rangle \sin(\zeta) \quad (25)$$

$$s_2 = \frac{n}{4\pi} \frac{\partial^2 B_y}{\partial x^2} \frac{l}{6B\rho} \langle \beta^{3/2} \rangle \cos(\zeta) \quad (26)$$

n is the number of sextupoles per family. Then,

$$s = \sqrt{s_1^2 + s_2^2} = \frac{n}{24\pi} \langle \beta^{3/2} \rangle \frac{\partial^2 B_y}{\partial x^2} \frac{l}{B\rho} \equiv \frac{n}{24\pi} \langle \beta^{3/2} \rangle K_2 l \quad (27)$$

And phasor rotation of the effective sextupole can be made by modulating ζ , which is now synonymous to χ from eq. 22. The phasor rotation causes a rotation of phase space at an observation point, so ζ can be tuned to give phase space the correct orientation at the extraction septa. Figure 15 in the Appendix is a demonstration of changing ζ to rotate the sextupole phasor and therefore the phase location of the effective sextupole in the ring.

In the Delivery Ring, straight sections 10 and 40 each contains a family of sextupoles, illustrated in Figure 14. In the ideal case a family of sextupoles will be separated by 60° per magnet—however, the straight cells in which the sextupoles live have a slightly larger phase advance. Therefore, each sextupole in a family only contributes approximately the same, and the two families are only approximately orthogonal by 30° . The phasors for the sextupoles in the Delivery Ring as compared to the theoretical phasors for orthogonal families is visually compared in Figure 2. Refer to Table 1 that shows the orthogonality of families; the coherent summations within each family are very acceptable, with the admixture of the off-component $< 2\%$.

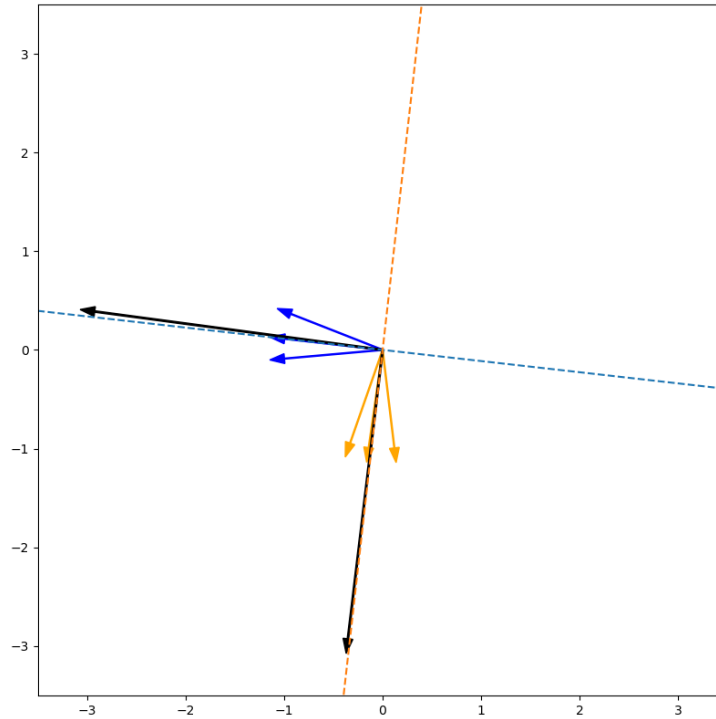


Figure 5. Phasor diagram for the sextupoles in the ring as found in Table 1. The x-axis is plotted $\cos 3\psi$ and the y-axis is $\sin 3\psi$. The two triplets of arrows correspond to the two families of sextupoles, and the sums of each family are the two large black arrows between the triplet. The dotted lines represent the slope of the phasors that represent the ideal phase advance between families. Lengths are normalized so each sextupole is unit length.

Sextupole	Polarity	β_x (m)	Lattice Phase	Ideal Phase	$\cos 3\psi$	$\sin 3\psi$
sss_10_3	-	13.3105	-64.98°	-60°	-0.96620	0.25781
sss_10_2	+	13.3100	0°	0	1	0
sss_10_1	-	13.3095	63.84°	60°	-0.97986	-0.19971
				Total →	2.94606	-0.05810
sss_40_1	+	13.3095	145.73°	150°	0.22172	0.97511
sss_40_2	-	13.3100	209.45°	210°	-0.02879	-0.99959
sss_40_3	+	13.3105	274.43°	270°	-0.22988	0.97322
				Total →	0.02063	2.94792

Table 1. Lattice function characteristics at orthogonal sextupole families. Phase angles are written with respect to sss_10_2 to show a case where $\cos 3\psi$ and $\sin 3\psi$ are clearly orthogonal, but it remains true that the two families will be orthogonal regardless of where phase angle ψ is measured from.

Phase space is intended to be in the upright position (Figure 7) at the electrostatic septum so that particles travel along the negative x direction for extraction, thereby minimizing particle losses on the septum wire. The value of $\zeta = \frac{\pi}{2}$ was determined to be a good choice, since fine-tuning the rotation for tracking does not carry over into the real-world in a meaningful way. In Figures 3-5, normalized phase space for 8000 protons with $\zeta = 80^\circ, 90^\circ$ and 100° is plotted to give a sense of what the chosen ζ looks like and how small modulations in ζ affect the rotation of phase space. Approximate separatrices are superimposed for visual aid.

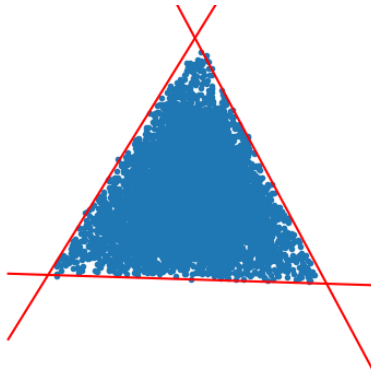


Figure 6. Normalized phase space at the electrostatic septum for $\zeta = 80^\circ$.

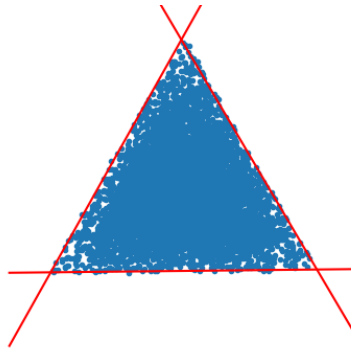


Figure 7. Normalized phase space at the electrostatic septum for $\zeta = 90^\circ$.

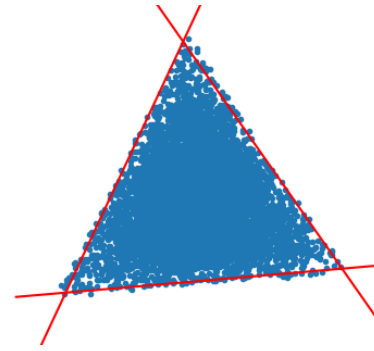


Figure 8. Normalized phase space at the electrostatic septum for $\zeta = 100^\circ$.

Sextupole Strength in Relation to Particle Losses

The particle losses incurred by ramping the sextupole strength from zero to s is characterized by normalized particle emittance $\epsilon_{f\%}$. For a radial distribution, $f\%$ is the percent of particles within radial distance $\sqrt{\epsilon}$. The starting distribution before the ramp was Gaussian, given by $\epsilon_{95\%} = 16\pi \text{ mm} - \text{mr}$. The normalized emittance of the distribution is associated with a circular area:

$$A = \frac{\pi\epsilon}{\beta\gamma} \quad (28)$$

$\epsilon / \beta\gamma$ is the geometric emittance and β and γ are relativistic factors.

Using the fixed points from equation 16, the total sextupole strength s (length of the phasor) gives area A of stable phase space:

$$A = \frac{\delta Q^2}{\sqrt{3}s^2} \quad (29)$$

As the tune separation decreases, the stable phase space shrinks, and at $\delta Q \rightarrow 0$, all particles become unstable, the mechanism that facilitates extraction. For the sake of determining s , however, δQ is considered constant.

Then, estimating losses in the beam due to the sextupole ramp for zero to s comes from comparing equation 28 to equation 29. Emittance is calculated from the area of the stable phase space triangle, and then compared to the starting distribution to give fraction of particles that are

stable:

$$f = 1 - e^{-3\epsilon/\epsilon_{95}}. \quad (30)$$

Sextupole ramp was simulated for several K_2l fields with 5000 particles, and 11 random seeds were used to generate a 95%-confidence interval on the remaining stable beam for each. Results are shown in Table 2 and Figure 9.

A trade-off is made between keeping the area of the beam small (prefers larger s) and minimizing initial losses from adiabatically ramping the sextupoles (prefers smaller s). Sextupole strength $s = 2.28 m^{-1/2}$ from sextupole field $K_2l = 1.18m^{-2}$ leaves roughly 95% of the initial beam emittance stable by simulation and was chosen as an optimal strength for tracking.

Stable Beam %	Theoretical Strength s $m^{-1/2}$	Simulated Strength s $m^{-1/2}$
97%	2.06	2.12
95%	2.23	2.28
93%	2.37	2.39-2.43
91%	2.49	2.51-2.55

Table 2. Theoretical and simulated sextupole strengths associated with percent stable beam.

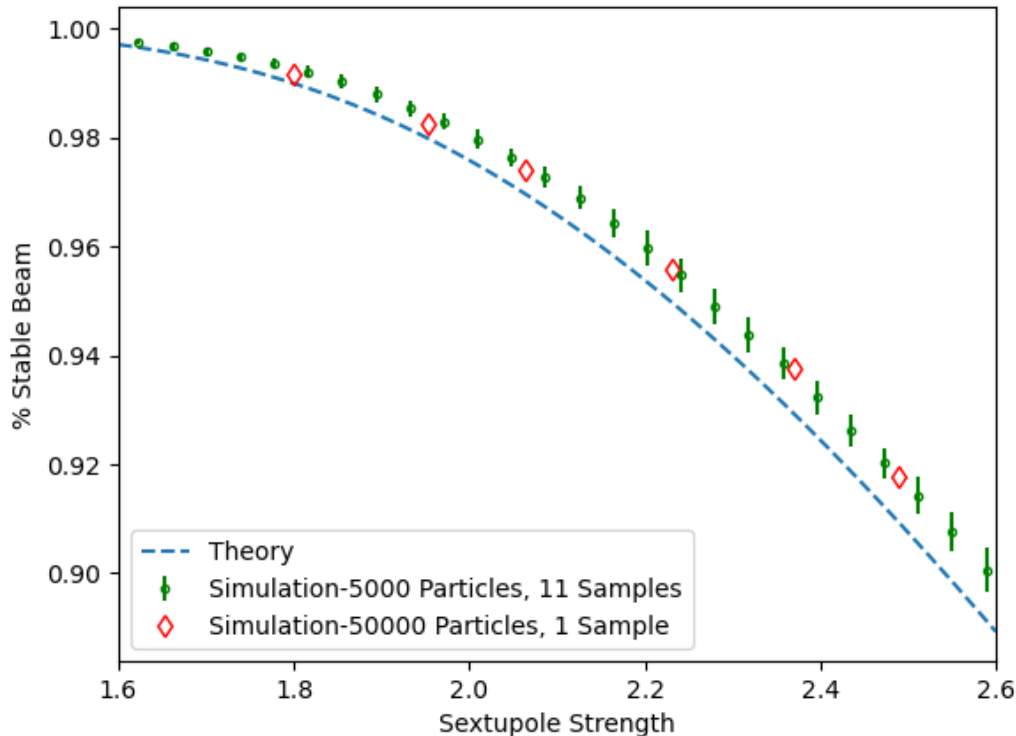


Figure 9. Fraction of stable beam after sextupole ramp as a function of sextupole strength s . Theoretical model is plotted from equation 30. Multiple simulation samples for 5000 particles are taken from different random seeds and their 95%-CI is plotted.

Placement of the Electrostatic Septum Wire

As tune separation Δ decreases to zero, particles slowly spill out along the separatrices. The electrostatic septum, placed at a negative horizontal offset (towards the outside of the ring in a right-handed coordinate system), extracts the particles that reach its wire plane by giving them a kick towards the outside. A lambertson magnet is placed downstream to complete extraction to the experimental target, but those details are not developed in this project. For illustrations of extraction at the (first) electrostatic septum, see Figures 12 and 13 and Figure 16 in the Appendix.

The step size ΔR gives the normalized coordinate phase-space distance a particle travels in three turns[10]:

$$\Delta R = R_2 - R_1 = \frac{9\pi s R_1}{1 - 9\pi s R_1} R_1 \quad (31)$$

where R_1 is the starting position and R_2 is the new position after three turns. The sextupole strengths are tuned so that extraction-phase space makes an upright triangle at extraction, as seen in Figure 4—so, ΔR can be used in just the horizontal plane: $\Delta R = \Delta x / \sqrt{\beta}$, $R_1 = x_1 / \sqrt{\beta}$, and $R_2 = x_2 / \sqrt{\beta}$. The inefficiency caused by particles hitting the septum wire is approximately:

$$ineff. = \omega \left(\frac{1}{x_s} + \frac{1}{\Delta x} \right) \quad (32)$$

ω is the wire width, x_s is the horizontal offset of the septum wires from the reference trajectory, and Δx is the step size given in the horizontal direction. Inefficiency is shown with respect to septum placement in Figure 11.

The inefficiency is monotonically decreasing with respect to step size, so larger step sizes are desirable in order to reduce losses at the septum. As a restriction, the step size Δx must not exceed the aperture of the electrostatic septum, $\Delta x \leq \text{apert.}$ otherwise particles will be lost on the mechanical body of the septum. This is physically illustrated in Figures 12 and 13. So, the maximum theoretical step size can be solved by letting:

$$\frac{\Delta x}{\sqrt{\beta}} = \frac{\text{apert.}}{\sqrt{\beta}} = \left(9\pi s \frac{x_s}{\sqrt{\beta}} \right) \left(1 - 9\pi s \frac{x_s}{\sqrt{\beta}} \right)^{-1} \frac{x_s}{\sqrt{\beta}} \quad (33)$$

Since the aperture restriction *apert.* is known to be 14 mm but the septum wire placement x_s is free, the equation is solved numerically for $x_s \approx 20.3$ mm to produce the maximum step size of 14 mm. To avoid scraping the conducting plane due to practical beam errors, an optimal value for septum wire placement during tracking was chosen to be 18 mm, which gives a step size of 12 mm. A graph of step size vs. septum offset with the aperture restriction can be found in Figure 8.

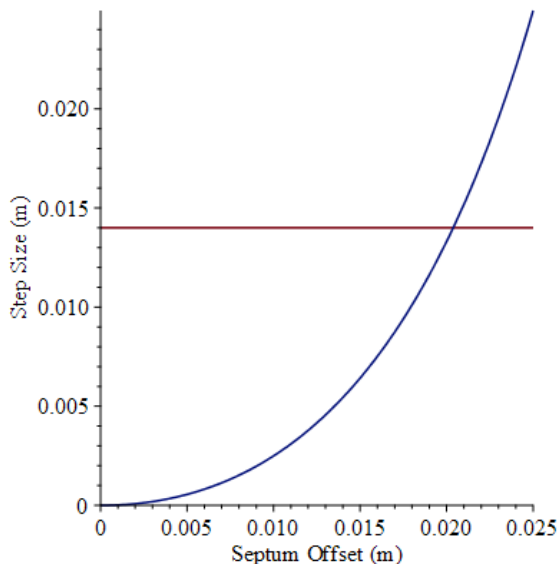


Figure 10. Step size as a function of septum offset x_s (blue). The horizontal line represents the aperture restriction, as step size $\Delta x \leq 14 \text{ mm}$. The lines intersect near septum offset $x_s = 20.3 \text{ mm}$. Sextupole strength was taken as $s \approx 2.28 \text{ m}^{-1/2}$ and $\omega \approx 1e - 4 \text{ m}$.

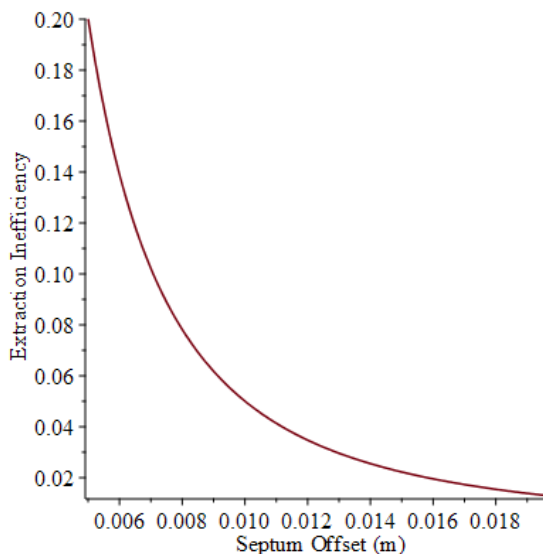


Figure 11. Extraction inefficiency $ineff.$ calculated as a function of septum offset x_s from combining equations 30 and 31. Inefficiency is only decreasing with respect to septum offset, demonstrating the motivation to maximize septum offset.

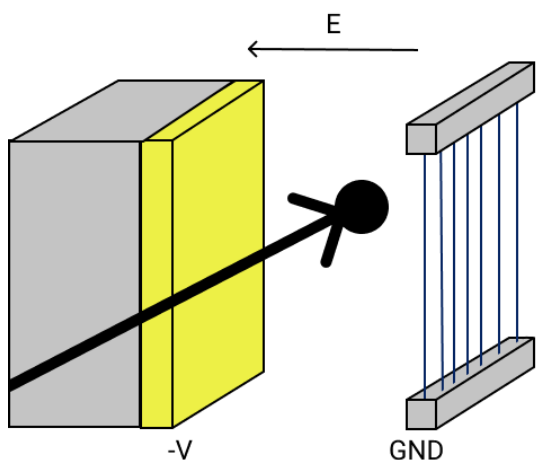


Figure 12. Illustration of the electrostatic septum. An electric field is established between a grounded wire plane and a conducting plate. Protons in the aperture are kicked in the direction of the field lines.

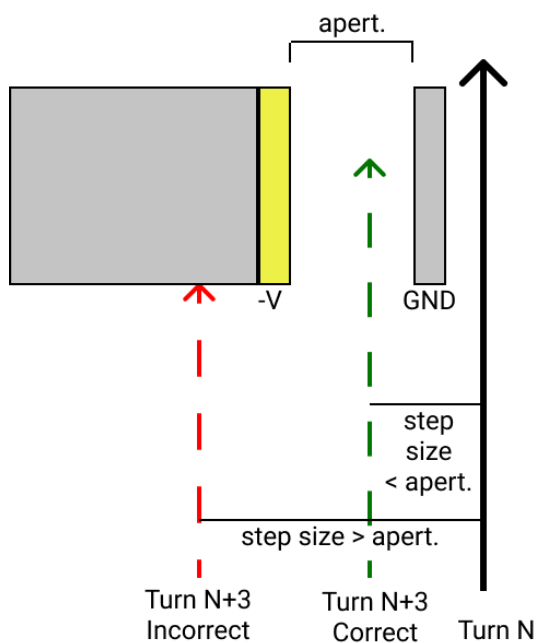


Figure 13. Visual explanation of why the step size cannot exceed the aperture of the electrostatic septum.

Simulation

Pictures of horizontal phase space from tracking with 25000 particles are shown in Figure 14. Sextupole strengths are ramped linearly to $K_2l = 1.18m^{-2}$ from turn 1-200 and 0th harmonic tune quadrupoles are ramped linearly to the third-integer machine tune from turn 1000-5000. The number of turns the quadrupole ramp takes place over can be modified to spill particles at a slower or faster rate. It is observed from tracking pictures that particles outside of the stable phase space triangle travel along the Hamiltonian separatrices, stable phase space shrinks to approximately zero as a function of turn number, and only a small fraction of particles reach the electrostatic septum at each turn, resulting in slow spill extraction.

Summary

This project established a tracking study for low-energy resonant extraction in the Delivery Ring that does not interfere with the current Mu2e extraction methods. The extraction process and its initial considerations as well as Delivery Ring-specific characteristics have been described. Values for sextupole family strengths and electrostatic septum placement are given to simulate slow spill extraction for an 800 MeV beam on the Delivery Ring lattice.

Acknowledgements

Thank you to my mentor, John Johnstone, and to John, Carol Johnstone and Jeff Eldred for teaching me what I know about particle accelerators, extraction, and the Delivery Ring. Also thank you to Adam Watts for showing his plotting code and to Alyssa Miller for help improving the pictures and the presentation.

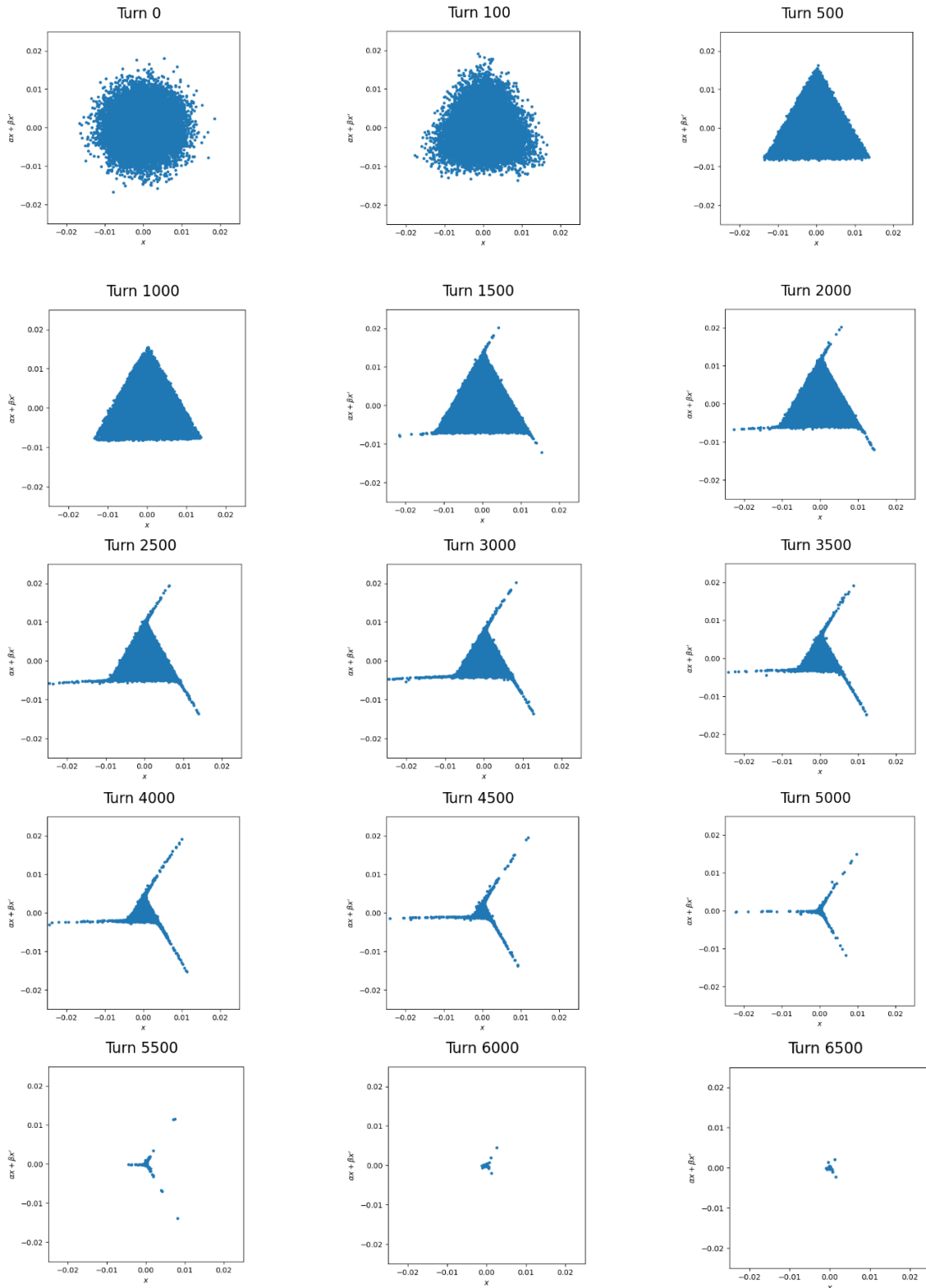
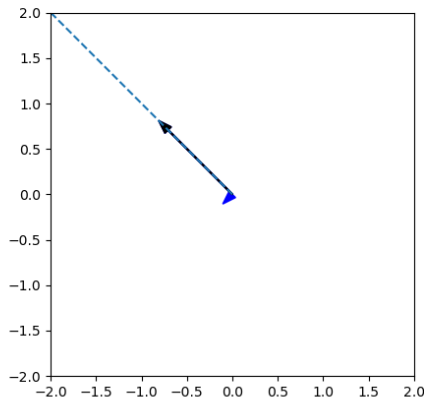


Figure 14. Picture book of horizontal phase space from tracking (25000 particles) as extraction is performed. Sextupoles are ramped linearly from turn 1-200, and 0th harmonic tune quadrupoles are ramped linearly from turn 1000-5000.

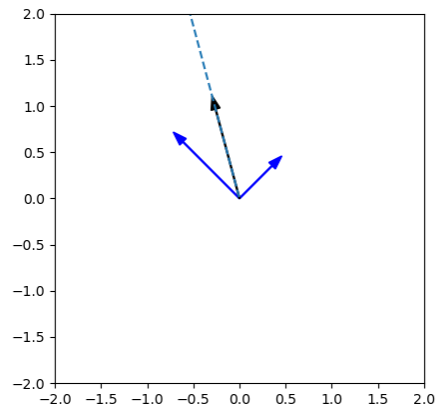
References

- [1] Fermilab Muon Department: <https://muon.fnal.gov/>
- [2] Delivery Ring: <https://www.fnal.gov/pub/science/particle-accelerators/accelerator-complex.html> or <https://operations.fnal.gov/displays/delivery.html>
- [3] Design Report Tevatron I Project, Fermilab-Design-1984-01, September 1984.
- [4] J.A. Johnstone & M.J Syphers, Delivery ring lattice modifications for transitionless deceleratio, Fermilab-Conf-16-509-APC, 2016.
- [5] G. Pezzullo, The Mu2e experiment at Fermilab: a search for lepton flavor violation. Fermilab-Conf-17-167-E, 2017.
- [6] D.A. Edwards, M.J. Syphers. *An Introduction to the Physics of High Energy Accelerators*. John Wiley & Sons, Inc. 1993.
- [7] L. Michelotti, J.A. Johnstone. Preliminaries towards studying resonant extraction from the Debuncher, Fermilab FN-0842-APC-CD, 2010.
- [8] MAD- Methodical Accelerator Design. <https://mad.web.cern.ch/mad/>
- [9] J. Eldred. Lecture 3C: "Nonlinear Resonances". USPAS June 2018 Classical Mechanics & Electromagnetism. <https://jseldredphysics.wordpress.com/uspas2018/>
- [10] J.A. Johnstone. An overview of third integer extraction (condensed). Beams-doc-5738.

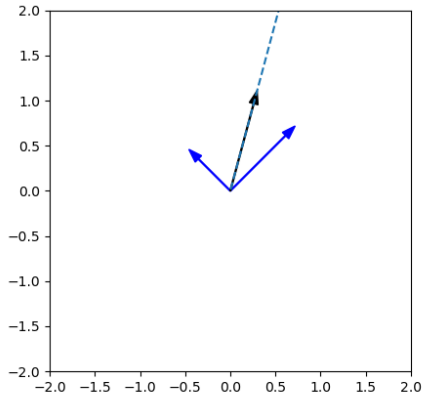
Appendix



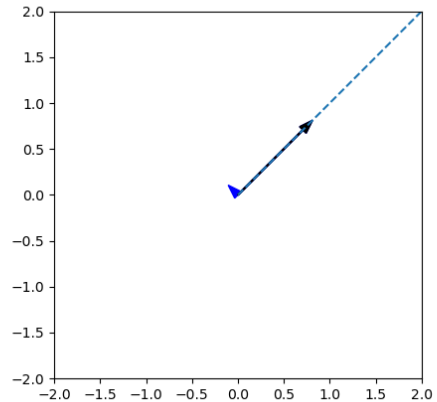
$$\zeta = 90^\circ.$$



$$\zeta = 120^\circ.$$



$$\zeta = 150^\circ.$$



$$\zeta = 180^\circ.$$

Figure 15. Example of sextupole phase rotation by modulating the amplitude of two orthogonal sextupoles or sextupole families. The black arrow with the dotted line pointing outwards gives the effect of the two sextupoles, while the two sextupoles are shown in blue (for the cases here $\zeta = 90^\circ, 180^\circ$, the net sextupole effect is completely made from an individual sextupole due to orientation, so the other won't be shown). The sextupole lengths are calculated $\sin(\zeta)$ and $\cos(\zeta)$ respectively (as normalized to unit length) while the phase angles (determined by positions in the ring) are held constant 30° apart. As representation of the orthogonal third-harmonic driving terms, amplitudes in the x and y direction are proportional to $\sin 3\psi, \cos 3\psi$. Here both phase angles are arbitrarily offset by 30° from the x-axis as an example, since initial phase offset depends on where the sextupoles are placed in the ring and where phase is being measured from.

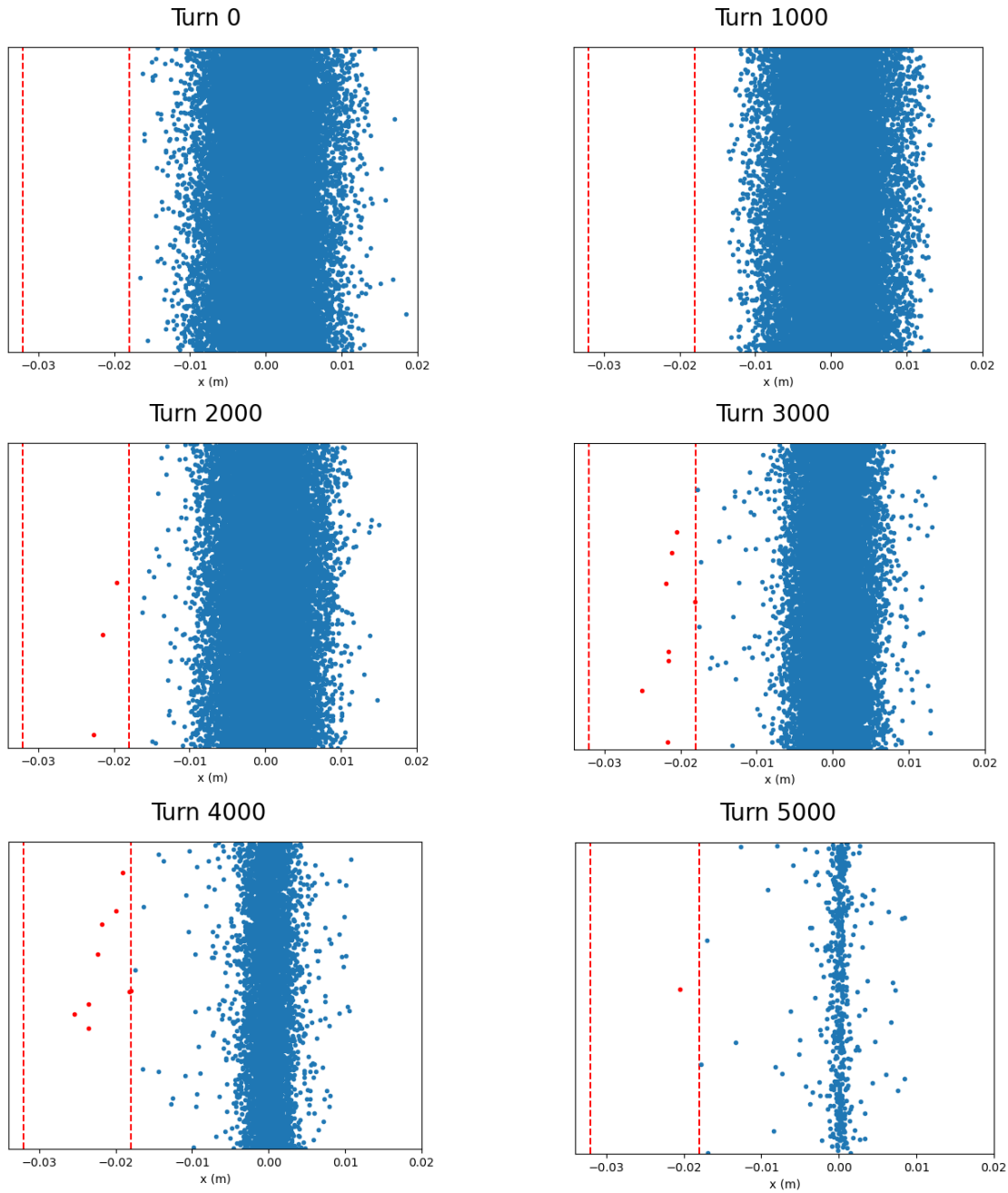


Figure 16a. Extraction snapshots of particles at the electrostatic septum. Each dot represents a particle from 25,000 particle tracking. The y-axis is random and used only for visual effect. The dotted vertical red lines represent the septum aperture, marking which particles will be extracted.

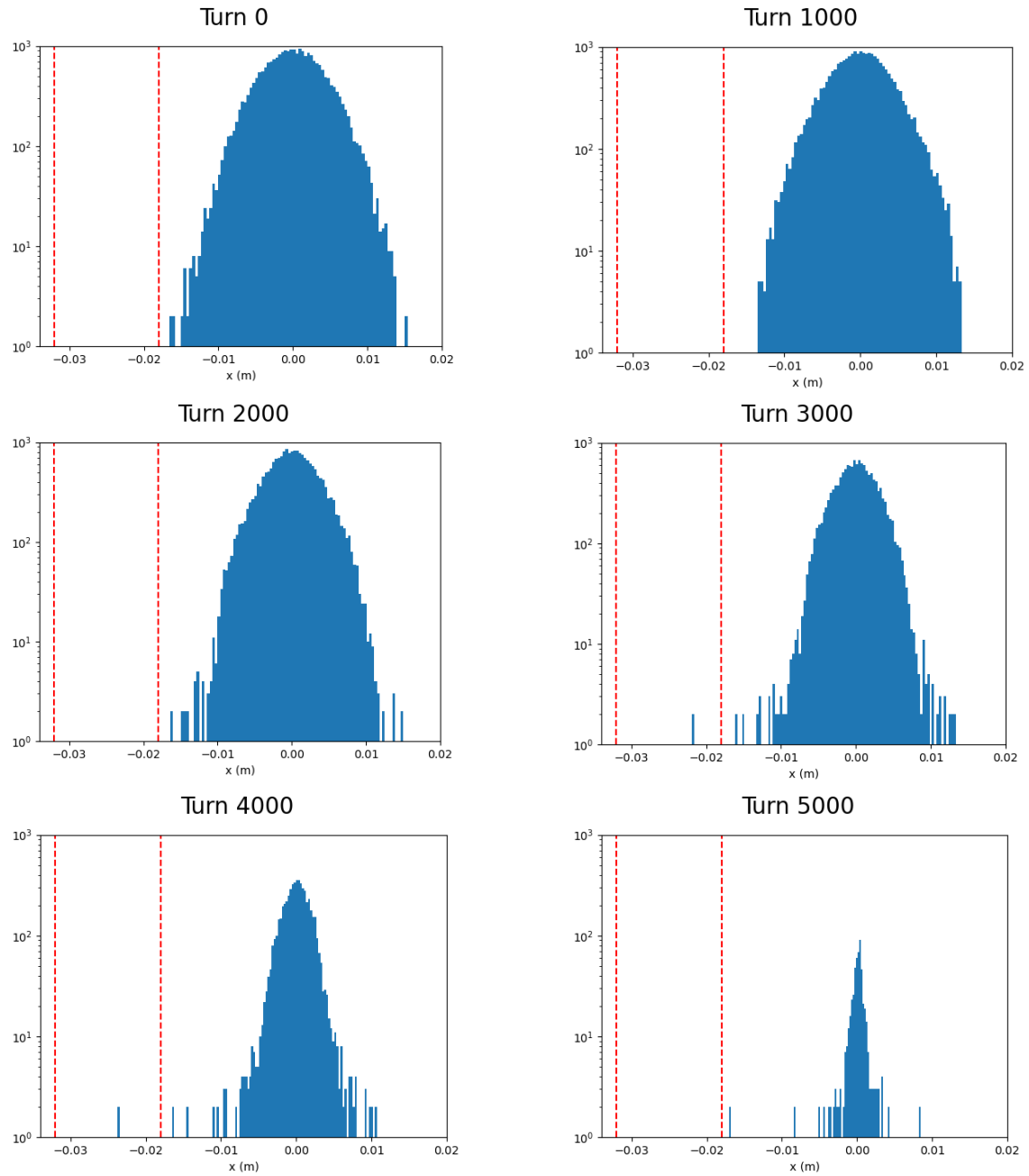


Figure 16b. Extraction snapshots of the transverse distribution at the electrostatic septum.